OPTICA

Structuring light waves in 3D volumes with high precision using communication mode optics

Vinicius S. de Angelis,[1,2,*] Ahmed H. Dorrah,[1,3] Leonardo A. Ambrosio,[2] David A. B. Miller,[4] and Federico Capasso[1]

[1]Harvard John A. Paulson School of Engineering and Applied Sciences, Harvard University, Cambridge, Massachusetts 02138, USA
[2]Department of Electrical and Computer Engineering, São Carlos School of Engineering, University of São Paulo, 400 Trabalhador são-carlense Ave., 13566-590, São Carlos, São Paulo, Brazil
[3]Department of Applied Physics and Science Education, Eindhoven University of Technology, Eindhoven 5612 AP, The Netherlands
[4]Ginzton Laboratory, Stanford University, Stanford, California 94305, USA
*viniciusangelis@seas.harvard.edu

Received 14 February 2025; revised 17 August 2025; accepted 18 August 2025; published 11 September 2025

Achieving precise control of light intensity in 3D volumes is highly in demand in many applications in optics. Various wavefront shaping techniques have been utilized to reconstruct a target amplitude profile within a 3D space. However, these techniques are intrinsically affected by cross-talk, which limits the quality of the reconstructed profile. We develop and experimentally demonstrate an approach that creates light waves with efficient energy distribution based on a linear superposition of the optimum orthogonal communication modes connecting a source plane and a receiving volume. We employ these modes to construct arbitrarily chosen 2D and 3D structured light waves with continuous depth of field within the output receiving volume and optically generate these waves using a spatial light modulator. Our generated intensity profiles exhibit a minimal level of cross-talk, great fidelity, and strong contrast. We envision our work to inspire new directions, to our knowledge, in any domain that requires controlling light intensity in 3D with high precision and also to serve as a benchmark for other wavefront shaping techniques.

https://doi.org/10.1364/OPTICA.559264

1. INTRODUCTION

Understanding how light interacts with matter is central to exploring the universe. High-resolution imaging through disordered media, for example, can reveal new insights into both cellular structures and distant galaxies. Similarly, the ability to manipulate, store, and detect light unlocks a wide range of photonic technologies, including quantum computing, communication, and sensing [1–7]. At the heart of these developments lies the need for tailoring the properties of incoming light in a nontrivial manner [8–13]. Early pursuits in structured light waves include the development of custom two-dimensional (2D) light intensity patterns at a particular transverse plane using modal bases such as Laguerre–Gauss, Hermite–Gauss, and Ince–Gauss modes [14–17], or by deploying iterative algorithms that solve inverse problems of light propagation, notably the Gerchberg–Saxton algorithm [18]. Although these methods provide control over the transverse field distribution at a given 2D plane, they lack control over the longitudinal beam profile. Tailoring the spatial and temporal properties of light over a 3D volume is a sought-after goal in many applications, including microscopy, spectroscopy, light–matter interactions, and optical sensing [19,20].

A variety of wavefront shaping techniques have been proposed and demonstrated for controlling light intensity in 3D, and the fundamental limitations of achieving a desired 3D distribution have been analyzed [21–33]. A common methodology employed in computer-generated holograms (CGHs) is to discretize a target 3D light distribution into a set of independent primitives. The incident waveform required to generate this target distribution is then synthesized by superposing the diffraction patterns from all the primitives in a given transverse plane. The techniques in this methodology are often classified based on the type of their primitive [34,35]. Point-cloud techniques, for instance, adopt a collection of source points, each emitting a spherical wave toward the transverse plane (CGH screen). The huge number of primitives involved in this method, however, mandates the use of look-up tables and optimization algorithms to reduce memory consumption [36]. Although polygon mesh techniques involve a relatively smaller number of primitives, they require an additional process of shading and texture mapping to maintain the quality of the reconstructed holograms, which inherently increases their computation time [37]. Multi-plane techniques mitigate this by adopting a set of parallel planes, uniformly spaced along the propagation direction. In this case, Fresnel diffraction or angular spectrum algorithms are implemented to compute the diffraction pattern from each plane [38–40]. These techniques have been widely adopted for creating 3D holograms, as they demand a significantly smaller number of primitives compared to point-cloud and polygon mesh techniques [41,42]. However, a limiting factor of these techniques is that

the depth of field of the transverse planes increases quadratically along the optical path. Consequently, the overlap of focal regions between adjacent planes often causes cross-talk, degrading the fidelity and quality of 3D reconstructions when the planes are evenly spaced. Although this interplane cross-talk can be reduced using optimization algorithms [43–47], a 3D reconstruction with high axial resolution is still challenging.

Wavefront shaping along the optical path can alternatively be achieved via a superposition of co-propagating Bessel modes with different longitudinal wavenumbers. By harnessing the spatial beating between these modes, one can modulate not only the intensity profile [48–50] but also other degrees of freedom of light along the propagation direction, including its total angular momentum [51–53] and its polarization [54]. By assembling many of these (nominally) non-diffracting light threads (uniformly spaced from each other) over a horizontal Cartesian plane, oriented parallel to the propagation direction, one can construct a 2D light sheet whose intensity profile can be controlled at will within the horizontal plane. By stacking several of those sheets within a volume, 3D structured light waves can also be synthesized [55–57]. Despite the continuous depth and axial resolution afforded by this technique, the energy distribution of a single light sheet has a large extent due to the multiple rings of the Bessel modes. This imposes a constraint on the minimum lateral separation between the light sheets for mitigating cross-talk, ultimately limiting the number of images that can be simultaneously projected with a fixed aperture. Convolutional neural networks have proven effective in reducing cross-talk only to a certain extent, i.e., in a simple case of only three light sheets with a low level of cross-talk [58]. In summary, creating 3D holograms with continuous depth of field and with densely spaced image planes, while maintaining minimum cross-talk, remains elusive.

In this work, we propose and experimentally demonstrate an approach to holography that addresses the above limitations. Using the singular value decomposition (SVD) modal optics [59], we compute the communication modes between two spaces, a source and a receiving space. The receiving space constitutes the 3D domain in which the target light intensity profile is defined. Meanwhile, the source space is a transverse plane where the required source waveform to reconstruct the target profile is computed as a linear superposition of the communication modes. We develop a procedure to encode the light waves from the source waveform in a CGH to be implemented by a phase-only spatial light modulator (SLM). Since the communication modes establish the optimum orthogonal channels connecting these two spaces, the required incident waveform leads to a light wave with the highest connectivity between the spaces, with the most efficient energy distribution in the receiving space. In principle, such optimal energy distribution of the individual modes produces 3D profiles with low cross-talk by ensuring that light is concentrated at the locations of interest. Communication modes for volume fields have previously been explored only in simplified theoretical cases—such as thin longitudinal volumes, spherical surfaces, or paraxial approximations using prolate spheroidal functions [60–64]. To our knowledge, this work presents the first comprehensive framework that unifies theory, numerics, and experiment for determining which arbitrary volume fields can be generated and how to realize them.

2. CONCEPT

First, we define the source and receiving spaces to compute the communication modes associated with these spaces. To do this, we describe the spaces as a collection of N_S source points and N_R receiving points, which results in each mode being described by a pair of eigenfunctions, one in the source space $|\Psi_{S,j}\rangle$ with dimension N_S and another in the receiving space $|\Phi_R\rangle$ with dimension N_R. The connection between the spaces is then established by a coupling operator G_{SR}, with dimensions $N_S \times N_R$, as illustrated in Fig. 1(a). For free-space operation, scalar Green's function provides an appropriate description for G_{SR} (see Section 6). The source and receiving eigenfunctions are then related to each other by $G_{SR}|\Psi_{S,j}\rangle = s_j|\Phi_R\rangle$, where s_j are the singular values computed from G_{SR}. The modulus squared of the singular values, $|s_j|^2$, namely coupling strengths, quantifies how efficiently each source eigenfunction $|\Psi_{S,j}\rangle$ creates its corresponding receiving eigenfunction. A full description of the communication mode theory is detailed in Section 6 and in Ref. [63].

We assume Cartesian coordinate systems (x_s, y_s, z_s) and (x_r, y_r, z_r) to describe the source and receiving spaces, and we separate the origins of these two coordinate systems by a longitudinal distance L. Then, we distribute source and receiving points to compose these spaces. Specifically, we arrange the source points as an array of $p_x \times p_y$ points in a transverse plane and space them from each other by distances d_x and d_y along the x_s and y_s directions, resulting in a source plane with dimensions $X_s = (p_x - 1)d_x$ and $Y_s = (p_y - 1)d_y$. Similarly, the receiving points are disposed in a 2D or 3D domain where we define their amplitude values according to a target light intensity profile $|\Phi_T|^2$. Figures 1(b)–1(d) show examples of receiving point distributions we explore in this work. In Fig. 1(b), the receiving points are distributed in the horizontal plane $y_r = 0$ as an array of $p_{x,r} \times p_{z,r}$ points. They are spaced from each other by distances $d_{x,r}$ and $d_{z,r}$ along the x_r and z_r directions, leading to a horizontal plane with dimensions $X_r = (p_{x,r} - 1)d_{x,r}$ and $Z_r = (p_{z,r} - 1)d_{z,r}$. A 3D distribution of receiving points is shown in Fig. 1(c), in which a set of $p_{y,r}$ horizontal receiving planes is uniformly spaced from each other by a distance $d_{y,r}$. Finally, a non-Cartesian distribution is depicted in Fig. 1(d). In this case, the receiving points are disposed in a set of $p_{z,r}$ rings placed along the optical axis, uniformly spaced from each other by a distance $d_{z,r}$, forming the lateral surface of a cylinder with radius R_r and longitudinal length Z_r. Along each ring, we uniformly place $p_{\phi,r}$ receiving points.

It is important to consider configurations of source and receiving spaces that provide a reasonable number of well-coupled modes, i.e., modes with sufficiently high coupling strengths. The values of all the parameters we adopted for each source and receiving point distributions of Fig. 1 are listed in Table 1. First, we fix the parameters of the receiving space and all the spacing distances. Next, we set the dimension X_s of the source plane to be slightly larger than that of the receiving space X_r. Finally, the separation distance L and the vertical dimension Y_s of the source plane are chosen to satisfy a criterion on the maximum allowed value for the source spacing distances d_x and d_y (see Supplementary Note 2 of Supplement 1). This criterion guarantees that the resulting wave created by the N_S source points over the entire receiving space is essentially the same as if we had a continuous source. In our examples, we set $L = X_s$ and then Y_s is determined by this criterion. The total number of horizontal planes we can allocate in the receiving space of Fig. 1(b) is constrained by our choice of the

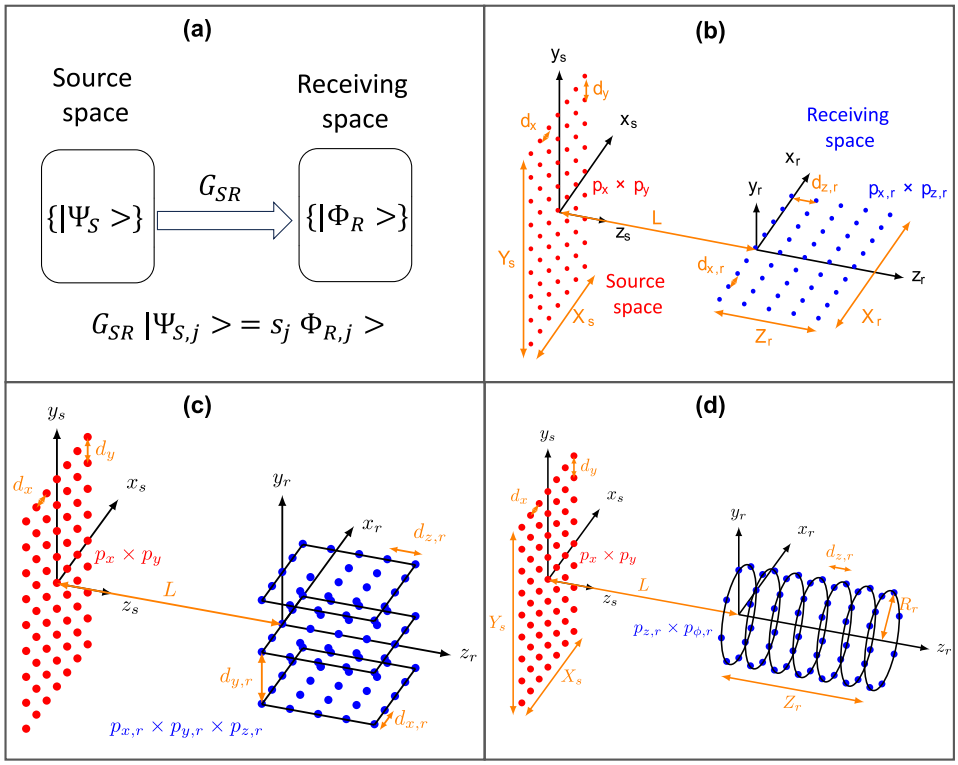

Fig. 1. General concept of communication modes and examples of source and receiving spaces. (a) Communication modes are established through a coupling operator G_{SR} between a source and a receiving space. These spaces are mathematically viewed as Hilbert spaces (H_S and H_R), each one containing a set of eigenfunctions ($\{|\Psi_S\rangle\}$ and $\{|\Phi_R\rangle\}$). In free space, G_{SR} is expressed by Green's function. Assuming a collection of N_S source points and N_R receiving points to describe these spaces, we can express G_{SR} as a $N_R \times N_S$ matrix. Examples of source and receiving space configurations in which the source points are distributed as an array of $p_x \times p_y$ points in a transverse plane and the receiving points as an array of: (b) $p_{x,r} \times p_{z,r}$ points in a horizontal plane, (c) $p_{x,r} \times p_{y,r} \times p_{z,r}$ points within a set of uniformly spaced horizontal planes, and (d) $p_{z,r} \times p_{\phi,r}$ points disposed within a set of uniformly spaced rings placed along the optical axis. In all these configurations, the spaces are separated by a distance L, an on-axis distance between their coordinate systems (x_s, y_s, z_s) and (x_r, y_r, z_r).

Table 1. Number of Source and Receiving Points, Their Spacing Distances, and the Longitudinal Separation between the Source and Receiving Spaces for Each Example of Source and Receiving Space Distributions of Fig. 1 [a]

	Source Plane			Receiving Space	
Distribution	$p_x \times p_y$	d_x, d_y	L	**Array of Points**	**Spacing Distances**
Fig. 1(b)	111×222	λ	110λ	$p_{x,r} \times p_{z,r} = 101 \times 101$	$d_{x,r} = d_{y,r} = d_{z,r} = \lambda$
Fig. 1(c)	111×301	0.5λ	50λ	$p_{x,r} \times p_{z,r} = 51 \times 51$	$d_{x,r} = d_{z,r} = \lambda$
				$p_{y,r} = 10$	$d_{y,r} = 15\lambda$
Fig. 1(d)	201×201	0.5λ	50λ	$p_{z,r} = 101$	$d_{z,r} = 0.5\lambda$
				$p_{\phi,r} = 101$	$R_r = 25\lambda$

[a]For the example of Fig. 1(d), we present the radius R_r of each ring that compose the receiving surface. The separation distance of the receiving points along each ring is $d_{\phi,r} = (2\pi/p_{\phi,r})\,R_r = 1.55\lambda$, which corresponds to an angular separation of 3.56°.

spacing distance $d_{y,r}$ and the aperture size Y_s. Finally, we show in Table 2 the memory storage and the computation time needed to compute the communication modes of the distributions of Fig. 1, parameterized according to Table 1.

For operation at $\lambda = 532$ nm, the coupling strengths $|s_j|^2$ in order of decreasing size of their magnitude associated with the distribution of Fig. 1(b) are shown in Fig. 2(a) for different values of the separation distance L and in Fig. 2(b) for different values of the source plane y-dimension Y_s (i.e., different values of p_y, keeping $d_y = \lambda$). Notice that the coupling strength values of the well-coupled modes in this distribution are closely characterized by a series of steps. Larger values of the source plane Y_s dimension and smaller values of L increase the number of steps. In addition, small L values also promote more modes in each step. After the series of steps, which for the red dashed curve of Fig. 2(b) is roughly

Table 2. Memory Storage and Computation Time Needed to Compute the Communication Modes of the Distributions of Fig. 1 Parametrized, as Listed in Table 1 [a]

Distribution	**Fig. 1(b)**	**Fig. 1(c)**	**Fig. 1(d)**
Number of modes	1300	4000	1000
Memory storage (GB)	0.516	3.09	0.657
Computation time (min)	105	712	166

[a]We deployed a dedicated server with processor Intel Xeon CPU ES-2690 0 at 2.90 GHz.

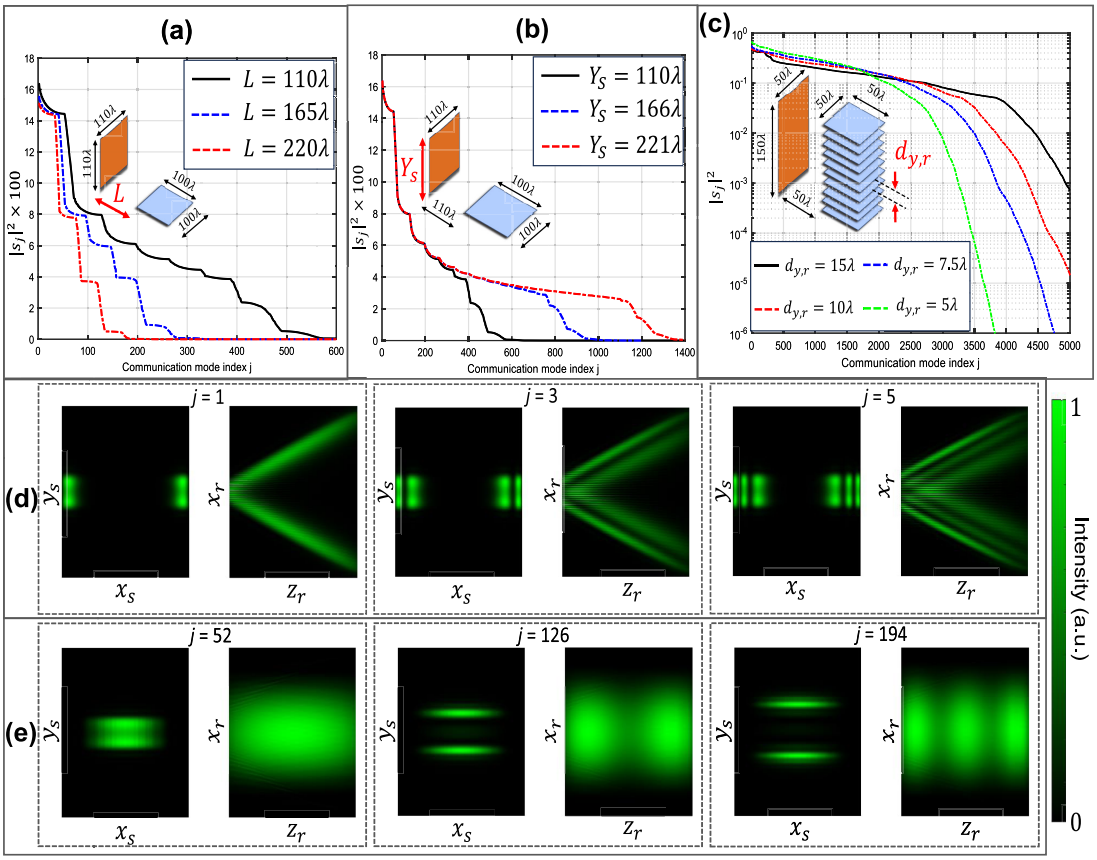

Fig. 2. Communication modes and their coupling strengths associated with a transverse source plane and a set of horizontal receiving planes. Coupling strengths in order of decreasing size of their magnitude of a single horizontal receiving plane computed at $\lambda = 532$ nm for (a) different values of the longitudinal separation distance L between the spaces and (b) for different values of the source plane y-dimension $Y_s = (p_y - 1)d_y$. The other parameters, which remained fixed, follow Table 1. The coupling strength curves are closely characterized by a series of steps after which the singular values decrease in a rapid fall-off fashion. The width of each step and the number of steps correspond, respectively, to the number of effective transverse and longitudinal modes. (c) Coupling strengths on a logarithmic scale for a set of 10 equally spaced horizontal planes for different values of spacing distances $d_{y,r}$ between them. Normalized squared amplitude of (d) the first three odd-numbered communication modes and (e) the last mode of each of the first three steps of the red dashed line of (b). In each sub-figure in (d) and (e), the source eigenfunction is shown on the left and its associated receiving eigenfunction on the right.

the region after the mode $j = 1200$, we find weakly coupled modes whose singular values decrease in a rapid fall-off fashion. This kind of fall-off, which limits the number of usable modes, is a universal behavior that was recently understood as following from the onset of a tunneling behavior of waves in and out of volumes [64]. Finally, Fig. 2(c) shows the coupling strengths $|s_j|^2$, in order of decreasing size of their magnitude of the distribution of Fig. 1(c), on a logarithmic scale for different values of the spacing distance $d_{y,r}$ between the horizontal planes. Notice that the number of well-coupled modes decreases for smaller values of $d_{y,r}$, imposing a fundamental constraint on the number of usable modes in this distribution.

The profiles of the source and receiving eigenfunctions associated with the distributions listed in Table 1 do not correspond to any of the standard beams (e.g., Bessel and Airy beams). To illustrate this, in Fig. 2(d), we show the normalized intensity profile of the first three odd-numbered communication modes associated with the red dashed curve of Fig. 2(b) at the source plane (on the left of each sub-figure) and at the receiving horizontal plane (on the right). As expected for this distribution, the intensity profiles of the source eigenfunctions are symmetric with respect to the $y_s = 0$ axis, where the horizontal receiving plane is located. Additionally, the intensity profiles of the modes give us insight to understand the coupling strength curve of this distribution. Specifically, the width of each step determines the number of effective transverse modes along the receiving plane x_r direction, while the number of steps corresponds to the number of effective longitudinal modes along the z_r direction. This is illustrated in Fig. 2(e), which shows the normalized intensity profile of the last mode of each of the first three steps of the red dashed curve of Fig. 2(b). Essentially, obtaining high longitudinal spatial frequencies in the horizontal receiving plane requires modes with lower coupling strengths. A complete analysis of the number of effective modes and how they are related to the parameters of the distribution of Fig. 1(a) is provided in Supplementary Note 3 of Supplement 1. This section also analyzes the intensity profiles of the communication modes and their coupling strengths for the other distribution examples of Fig. 1. Additionally, the intensity profiles of the first well-coupled communication modes associated with these distributions are shown in Visualization 1, Visualization 2, and Visualization 3.

Next, we structure light waves in the receiving spaces of the distributions shown in Figs. 1(b)–1(d). We begin by representing the target profile as a vector of amplitudes at the receiving points. This vector is then decomposed onto the receiving space basis. Finally, at the source space basis, we compute the corresponding source function by superposing the source components that generate each

receiving contribution of the target profile. This concept of synthesizing light waves using communication modes, first proposed in Ref. [32], is detailed in Section 6. Since the required source function $|\Psi_T\rangle$ is inversely proportional to the singular values s_j, adding weakly coupled modes results in extremely large source amplitudes. This hinders the efficient generation of the resulting light wave, in practice, due to limitations imposed by the SLM's phase modulation depth, as will be shown in Section 4 . Nevertheless, the use of weakly coupled communication modes has been related to passing conventional diffraction limits [63], being consistent with sub-diffraction imaging, which requires large source amplitudes to image sub-diffraction features [65]. Therefore, for a physically realizable source solution, we incorporate only the well-coupled communication modes in the summation of Eq. (3), identified here as the first M communication modes, ranked by decreasing order of their coupling strengths. The value of M for a given distribution is roughly estimated from the rapid fall-off in the coupling strength curve. Equivalently, as the sum of the coupling strengths is finite, bounded by a sum rule S (see Supplementary Note 1 of Supplement 1), we can choose a number M of modes that nearly provide S, avoiding the incorporation of modes ($j > M$) with negligible coupling strengths. As noticed in Ref. [32], the evaluation of this number M of well-coupled modes gives us a definition of the number of effective degrees of freedom within a receiving space to construct feasible 3D light waves in that space.

Projecting the entire content of the target amplitude profile onto the range of well-coupled modes of the receiving space set is generally not possible for the distributions of Figs. 1(b)–1(d) when the target phase is a free parameter. Thus, to obtain a physically realizable source function, we need to specify a phase front to modulate the target amplitude profile. Here we adopt a phase front of the form $\exp(\mathrm{i}Qz_r)$, in which Q is a positive real constant with $Q \leq k = 2\pi/\lambda$. We do this because we understand that any wave we generate from our source plane is physically going to have predominantly some underlying phase variation along the longitudinal direction, and so we can only reasonably generate patterns that have a similar underlying phase variation. This plane wave phase front is the simplest one that provides this variation since now the waves from the source are subjected to a propagation with longitudinal wavenumber given by the parameter Q, and thus with an angle of $\theta = \cos^{-1}(Q/k)$ with respect to the longitudinal direction. With this phase front, the intensity profile of the source function is localized around the vertical positions $Y_{T,s} = \pm(L + Z_r/2)\tan[\cos^{-1}(Q/k)]$ in the source plane. To illustrate this procedure, we consider the configuration of the receiving and source space depicted in Fig. 3(a), parameterized according to Table 1, and the binary 2D image shown in Fig. 3(b) as our target receiving intensity profile $|\Phi_T|^2$. Adopting $Q = 0.95k$, the entire content of this target profile is projected onto the range of the first 1200 coupled modes, as depicted in Fig. 3(c), which shows the inner product coefficients between the receiving eigenfunctions $\{|\Phi_{R,j}\rangle\}$ and the modulated target profile $\Phi_T \exp(\mathrm{i}Qz_r)$ by the blue dots. For reference, we also show in this plot the coupling strengths $|s_j|^2$ (in arbitrary units) in a red dashed line. Figure 3(d) shows the squared amplitude of the required source function $|\Psi_T|^2$ and the resulting wave intensity $|\phi|^2$, calculated using the first 1200 modes. This value of Q yields $Y_{T,s} = \pm 52.59\lambda$, which corresponds to the vertical positions occupied by the source function ($\approx \pm Y_s/4$) and results in a fully reconstructed profile in the receiving horizontal plane.

Finally, notice that the incorporation of the phase front $\exp(\mathrm{i}Qz_r)$ increases the extent ΔY of the source profile along the source plane y_s dimension. As reconciled with the intensity profiles of the modes of this distribution at the source plane, a higher extent along the source plane y_s dimension creates waves with high longitudinal spatial frequencies in the receiving space. In Supplementary Note 4 of Supplement 1, we relate the extent ΔY of the source profile to the characteristic minimum length of the wave field (minimum spot) Δz that we can create along the longitudinal direction at a certain position z_0 from our finite source transverse aperture. Additionally, the incorporation of the plane wave phase front is analyzed for different values of Q in Supplementary Figure S9 of Supplement 1.

3. EXPERIMENTAL GENERATION

We optically reconstructed light waves at operating wavelength $\lambda = 532$ nm using a phase-only reflective SLM (SANTEC 200) with a pixel pitch $\delta = 8$ μm. Because the SLM only modulates the phase of the incident wavefront, it cannot act as the source plane of the configurations of Fig. 1, which assume self-propagating light from the source. Instead, the SLM serves as a platform where the resulting waves from the complex amplitude source profiles are encoded into a phase mask. In this encoding process, we aim for a high reconstruction accuracy of the wave solutions computed via SVD. To encode on the SLM the wave solutions computed from the distributions listed in Table 1, first, as illustrated in Fig. 3(e), we compute the resulting wave at the plane $z_s = L$, i.e., $\phi(x_s, y_s, L)$ from the required source function using Eq. (4), and we scale it up to match the utilized SLM display area. We then convert its complex field into a phase-only mask using a phase CGH encoding algorithm. Finally, we add a blazed grating profile to the phase-only mask to operate off-axis, separating the hologram's spectrum from the SLM zeroth diffraction order in k space. Our experimental setup is shown in Fig. 3(f). The laser beam is first expanded and collimated to illuminate the utilized SLM display area as a uniform plane-like wave. After the SLM, we place a standard $4f$ lens system whose purpose is to recover the complex field $\phi(x_s, y_s, L)$ at the front focal plane of the second lens. The first lens performs a Fourier transform operation, projecting the phase mask spectrum (which contains both amplitude and phase information) at the Fourier plane, i.e., at the mutual focal point plane of the two lenses. In this plane, we place an iris to spatially filter the desired spectrum, encoded on the first diffraction order of the incoming beam, while blocking the undesired zeroth diffraction order in k-space. The second lens performs an inverse Fourier operation, transforming the filtered spectrum into real space, recovering the complex field $\phi(x_s, y_s, L)$ in the front focal plane of this lens. Finally, using a CCD camera mounted on a translational stage, we record transverse intensity distributions of the resulting wave at different z_r positions. Stacking these transverse distributions, we obtain the optical reconstruction of the resulting wave intensity.

We implemented a phase CGH encoding algorithm that transforms an input scalar complex field into a phase CGH with high accuracy using a lookup table. Its methodology is described in Ref. [66] and in Supplementary Note 5 of Supplement 1. The high performance of this algorithm comes at the expense of providing a relatively low diffraction efficiency, as the intensity of the high-order diffraction contributions of the phase mask spectrum is significantly reduced (see Supplementary Note 5 of Supplement 1). However, from the output of the $4f$ system onward, the energy

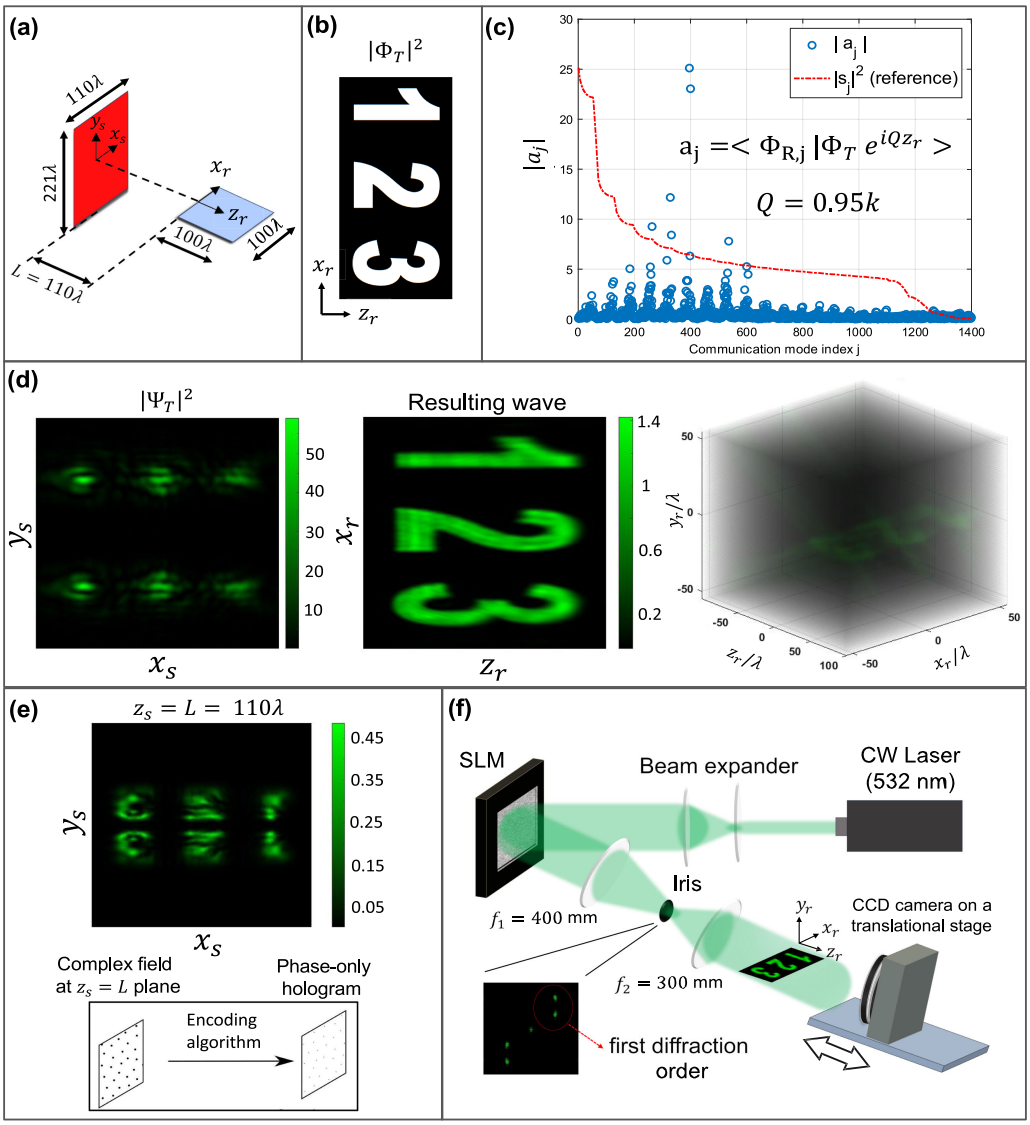

Fig. 3. Optical reconstruction of structured light waves based on communication modes using a reflective phase-only SLM. For a given source and receiving space configuration (a), we compute the associated communication modes and their coupling strengths. (b) We define a target light intensity distribution (c) and project it onto the set of receiving eigenfunctions. (d) We compute the required source function Ψ_T at the source plane and its associated resulting wave ϕ within the receiving space. (e) Encoding process: we evaluate the resulting wave from the required source profile at the plane $z_s = L$, scale it up to match the utilized SLM display area, and convert its complex field distribution into a phase-only CGH by means of a phase CGH encoding algorithm. (f) Optical setup: after the SLM, we employ a standard $4f$ lens system to recover the complex field $\phi(x_s, y_s, L)$ at the front focal plane of the second lens. At the Fourier plane (mutual focal point plane of the two lenses), an iris is used to filter the desired spectrum (encoded on the first diffraction) and to block the unmodulated SLM zeroth diffraction order. A CCD camera on a translational stage records transverse intensity distributions of the resulting wave at different longitudinal positions.

is transmitted through the optimal communication channels. Finally, the reason why we encoded the resulting wave at the plane $z_s = L$ instead of directly encoding the required source function (at the plane $z_s = 0$) is because the source functions related to the distributions listed in Table 1 are generally complicated complex-valued functions with high variations and oscillations in amplitude. When these functions are implemented in the phase mask and encoded on the SLM, they are not fully reconstructed after the $4f$ system due to the finite SLM pixel pitch. In contrast, the resulting wave at $z_s = L$ is a smooth function with lower variations in amplitude, leading to high-accuracy reconstruction by the SLM. In Supplementary Figure S11 of Supplement 1, we encode the resulting wave at different longitudinal distances from the source plane and evaluate the mean squared error between that wave and the one recovered after the $4f$ system. Encoding the wave solution at the plane $z_s = L$ onto the SLM enables high-fidelity reconstruction of the SVD-computed solution, with minimal mean squared error.

Because the wave solutions computed from the distributions listed in Table 1 are scaled up to match the utilized SLM display area, the 1:1 aspect ratio of our original (simulated) light wave in the receiving space is not preserved in our optically reconstructed light waves. This results in waves that are substantially stretched along the propagation direction. This is not a fundamental limitation of our approach but rather a technical one because of the use of an SLM, which has a large pixel pitch compared to the incident

wavelength ($\delta \approx 15\lambda$). Metasurfaces, with their subwavelength pixel pitch, would allow us to encode the wave solution without any magnification, thus preserving the original 1:1 aspect ratio. However, a drawback of a metasurface is its lack of tunability. Different metasurfaces need to be fabricated to create distinct target intensity profiles. In our implementation, the utilized SLM display area was set to occupy 600 pixels along the vertical direction, resulting in a magnification of $9007.519\lambda/Y_s$ for the encoded CGH. For details on the aspect ratio of our reconstructed light waves and how a 1:1 aspect ratio could be achieved by means of a de-magnification $4f$ system, see Supplementary Note 6 of Supplement 1. Finally, since the computation time and memory storage of the communication modes associated with our considered distributions described by Table 1 are already quite large, as presented in Table 2, performing the SVD computation for scaled versions of these distributions becomes highly unfeasible. To give a perspective, scaling the dimensions of the distribution shown in Fig. 3(a) by a factor of $\alpha = 40.5$ to match our utilized SLM display area leads to an SVD problem with an estimated number of almost 1,619,000 well-coupled modes, requiring a memory storage of around 132 TBytes (see Supplementary Note 7 of Supplement 1 for details).

4. RESULTS

First, examples of different 2D structured light waves, using the first 1200 communication modes associated with the distribution of Fig. 3(a), are presented in Fig. 4. On the left of each sub-figure, we show the target receiving amplitude $|\Phi_T|$; in the middle, the simulated resulting wave intensity $|\phi|^2$ in the receiving horizontal plane; and on the right, the optically reconstructed wave using the optical setup of Fig. 3(f). In all the examples, the target profile is modulated by a phase front $\exp(\mathrm{i}Qz_r)$ with $Q = 0.95k$, leading to source functions localized around $\approx \pm Y_s/4$ at the source plane. Figures 4(a) and 4(b) exhibit examples of target binary images containing bright digits on a dark background, while examples involving dark geometric shapes on a bright background and a checkerboard pattern are shown in Figs. 4(c) and 4(d), respectively. In Table 3, we evaluate metrics to quantify the reconstruction quality of these measured holograms, compared to their target profiles, including mean squared error (MSE), Michelson contrast, uniformity of the illuminated regions, and signal-to-background ratio (SBR). The diffraction efficiency of these holograms is also presented in Table 3. Notice that our approach provides reconstructed patterns with great fidelity, strong contrast, and good uniformity. In particular, our measured holograms present MSE values lower than those of holograms created from the HoloTile modality, such as the TMultiplexing-Tile hologram applied to volumetric printing in Ref. [67], which has an MSE around 0.09 for the reconstructed profile of a letter "A."

An example involving a target grayscale image containing features with high spatial frequencies is provided in Fig. 4(e). Notice that the fine rectangular features located in the middle of the receiving plane (which represent the raindrops) present a better reconstruction than the rectangular features located at the end of the receiving plane (which represent the sun rays). This phenomenon is intrinsically due to the finite dimension Y_s of our source aperture and is independent of the modes (or basis functions) used to create the structured light wave. In particular, the characteristic minimum length of the wave field Δz that our (finite) source aperture can create varies along the longitudinal

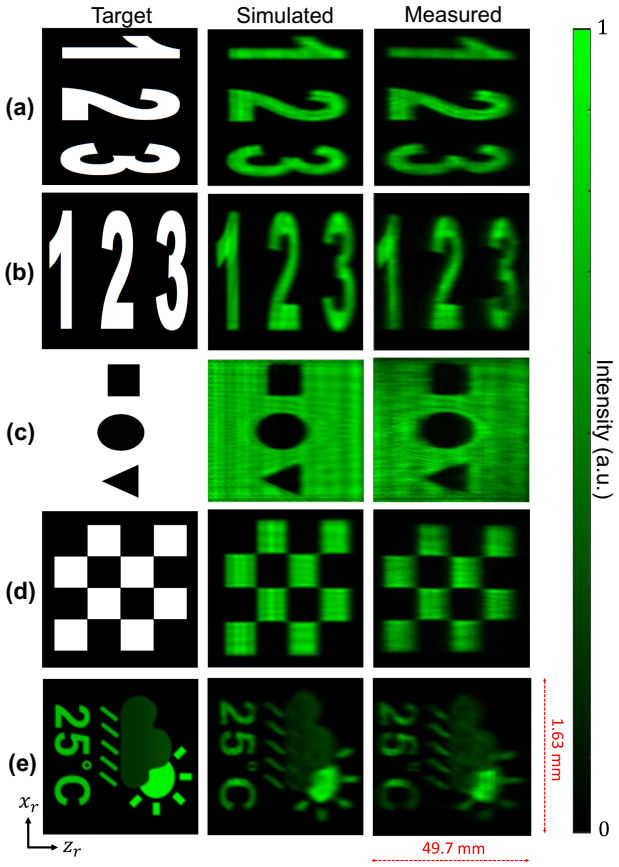

Fig. 4. Examples of 2D structured light waves projected in a horizontal receiving plane. These waves are computed from the first 1200 well-coupled communication modes associated with the source and receiving space configuration of Fig. 1(b) with parameters listed on Table 1. From left to right: target receiving amplitude, simulated resulting wave intensity at the receiving horizontal plane, and optical reconstruction of the resulting wave using a phase-only SLM. (a), (b) Bright digits on a dark background with distinct orientations. (c) Dark geometric shapes on a bright background. (d) A checkerboard pattern. (e) A grayscale image. Since the wave solutions are scaled up to match the utilized SLM display area, the 1:1 aspect ratio of the simulated waves is not preserved in the measured results. Their measured dimensions are $Z_r \times X_r = 49.7\ \text{mm} \times 1.63\ \text{mm}$.

position z_r of the receiving space, being higher for points located further away from the source plane (Supplementary Note 4 of Supplement 1). To fully resolve these fine features in our wavefront shaping method, we would need to consider a source plane with a higher dimension Y_s and with a denser array of source points for this additional increment in the dimension Y_s to satisfy the criteria for the source spacing distances (Section 2 of Supplement 1). Additionally, the target profile must be modulated by a plane wave phase front $\exp(\mathrm{i}Qz_r)$ with a lower value of Q so that the required source function has a higher extent at the source plane.

Next, we present examples of 3D structured light waves computed using the first 3500 modes associated with the source and receiving space distribution of Fig. 1(c), parameterized as listed in Table 1. First, we project simultaneously eight distinct digits, from "1" to "8," assigning each digit a binary amplitude profile to one of the eight inner horizontal receiving planes. In Fig. 5(a), we show the target intensity profile $|\Phi_T|^2$ and the intensity of the corresponding required source function $|\Psi_T|^2$. The optical reconstruction of the resulting wave implemented on the SLM is

Table 3. Accuracy and Reconstruction Quality Metrics of the Measured 2D Holograms of Figs. 4(a)–4(d) and Their Diffraction Efficiency[a]

Metrics	Fig. 4(a)	Fig. 4(b)	Fig. 4(c)	Fig. 4(d)
Mean squared error (MSE)	0.0256	0.0466	0.0475	0.0388
Contrast: $(I_{max} - I_{min})/(I_{max} + I_{min})$	0.994	0.996	0.9736	0.991
Mean value of bright regions: $\bar{I}_b$	0.923	0.867	0.964	0.933
Uniformity of bright regions: $1 - \sigma_{I_b}/\bar{I}_b$	0.757	0.711	0.789	0.7414
Mean value of dark regions: $\bar{I}_d$	0.0561	0.0969	0.163	0.0881
Signal-to-background ratio (SBR): $\bar{I}_b/\bar{I}_d$	16.55	8.95	5.90	10.59
Diffraction efficiency	2.11%	2.66%	4.12%	2.85%

[a]Bright regions (i.e., illuminated regions) are defined as the ones in which the normalized measured intensity is $I \geq 0.5$. Similarly, dark regions are those in which $I < 0.5$. The parameter σ_{I_b} refers to the standard deviation of the bright regions.

shown in Fig. 5(b), in which we can clearly identify and distinguish all the eight digits, indicating the low level of cross-talk between their reconstructed intensity profiles. This can also be noticed from the measured transverse planes of the optical reconstruction as seen in the same figure at the mid ($z_r = Z_r/2$) and quarter ($z_r = Z_r/4$) longitudinal distances. In Fig. 5(c), we compare the measured and simulated results of the structured light wave intensity in all the eight inner horizontal receiving planes. The reconstructed digits have great fidelity with a mean MSE of 0.0556, a mean Michelson contrast of 0.944, and a mean uniformity of the illuminated regions of 0.7345. See Supplementary Note 8 of Supplement 1 for the values of these metrics in each horizontal plane. The diffraction efficiency is 1.66%. An additional example of a structured light wave involving the projection of eight layers of an ellipsoid is provided and discussed in Supplementary Note 9 of Supplement 1. In both cases, the phase front applied to the target profile is $\exp(\mathrm{i}Qz_r)$ with $Q = 0.95k$.

The example of Fig. 5 highlights the strength of our approach in generating structured light fields with continuous depth of field, high contrast, and minimal cross-talk across eight horizontally spaced planes, each separated by just 0.359 mm in our optical setup. In contrast, shaping light fields across the same planes using the light-sheet wavefront shaping method results in significant cross-talk between adjacent planes. This comparison is detailed in Supplementary Note 10 of Supplement 1, where we evaluate the level of cross-talk in all the eight horizontal planes shown in Fig. 5. For a fair comparison, the light sheets were designed using the same optimized parameters reported in Ref. [57], with CGHs generated via the same SLM and phase CGH encoding algorithm employed in our method. To substantially reduce cross-talk in the light-sheet approach, the planes must be spaced approximately 3 mm apart at the SLM plane (see Ref. [57]). However, this spacing constraint limits the number of projectable planes to just four, due to the 9.6 mm aperture size of the SLM. In contrast, our method achieves a significant improvement not only by minimizing cross-talk but also by enabling the projection of more image planes within the same aperture. Specifically, our system reconstructs eight cross-talk-free planes over a vertical range of 2.5 mm (3.2 planes/mm), compared to only four planes over 6.75 mm (0.59 planes/mm) in the light-sheet method, demonstrating enhanced vertical resolution in 3D holography.

Since the feasible 3D light waves that can be constructed in a given receiving space are constrained by the number of well-coupled modes supported in that space, we can determine fundamental constraints in 3D distributions that hinder the reconstruction of desired intensity profiles. For the distribution of Fig. 1(c), a constraint is imposed by the spacing distance $d_{y,r}$ between the horizontal planes, as smaller values of $d_{y,r}$ lead to a reduced number of well-coupled modes [see Fig. 2(c)]. For a separation distance of $d_{y,r} = 7.5\lambda$, the target intensity profile applied in the example of Fig. 5 is not accurately reconstructed using only the well-coupled modes. In Supplementary Figure S17 of Supplement 1, we show the source function intensity profile and the simulated resulting wave computed from the first 3500 modes and the first 4500 modes. Notice that, although the incorporation of weakly coupled modes provides a full reconstruction of the target profile in simulation, the intensity of the source function acquires extremely high intensity variations, with its peak value reaching more than 2200 times higher than that in the receiving planes. The SLM is not able to recover the resulting wave from this high-energy source function after the $4f$ system due to its finite phase modulation depth, leading to reconstructed profiles with significant distortions, as shown in Supplementary Figure S18 of Supplement 1. Ultimately, creating highly densely packed 3D light structures (very small $d_{y,r}$ values) requires passing conventional diffraction limits and thus the use of sub-diffraction systems for a full reconstruction.

Finally, an example of a structured light wave projected onto the cylinder surface of Fig. 1(d) and parameterized as listed in Table 1 is presented in Section 11 of Supplement 1. The generation of light waves along a body with rotational symmetry using a multi-plane approach [68] leads to reconstructed waves with low resolution along the longitudinal direction. Our results, on the other hand, show reconstruction of an arbitrary intensity profile with continuous depth of field. Moreover, the intensity distribution of the light wave is well localized around the cylinder surface with a complete dark intensity around the optical axis over the entire longitudinal distance of the cylinder.

5. DISCUSSION

We introduced and experimentally verified a new approach to holography based on a linear superposition of the optimum orthogonal communication modes connecting a source plane and a receiving volume. Each communication mode encompasses a pair of eigenfunctions, one in the source space and another one in the receiving space, both computed by means of singular value decomposition modal optics. The high connectivity provided by these modes renders 2D and 3D structured light waves with highly localized energy distribution and a minimal level of cross-talk. As a consequence, these waves can be perceived from different angles, and thus are potentially employed in volumetric displays and AR/VR headsets. Additionally, our method could be favored in applications that require controlling light's intensity within a 3D domain with high precision and contrast, notably in materials processing, optical trapping, and bioprinting [69]. Other potential applications include its implementation in point spread function engineering to improve the imaging performance of optical systems [70,71].

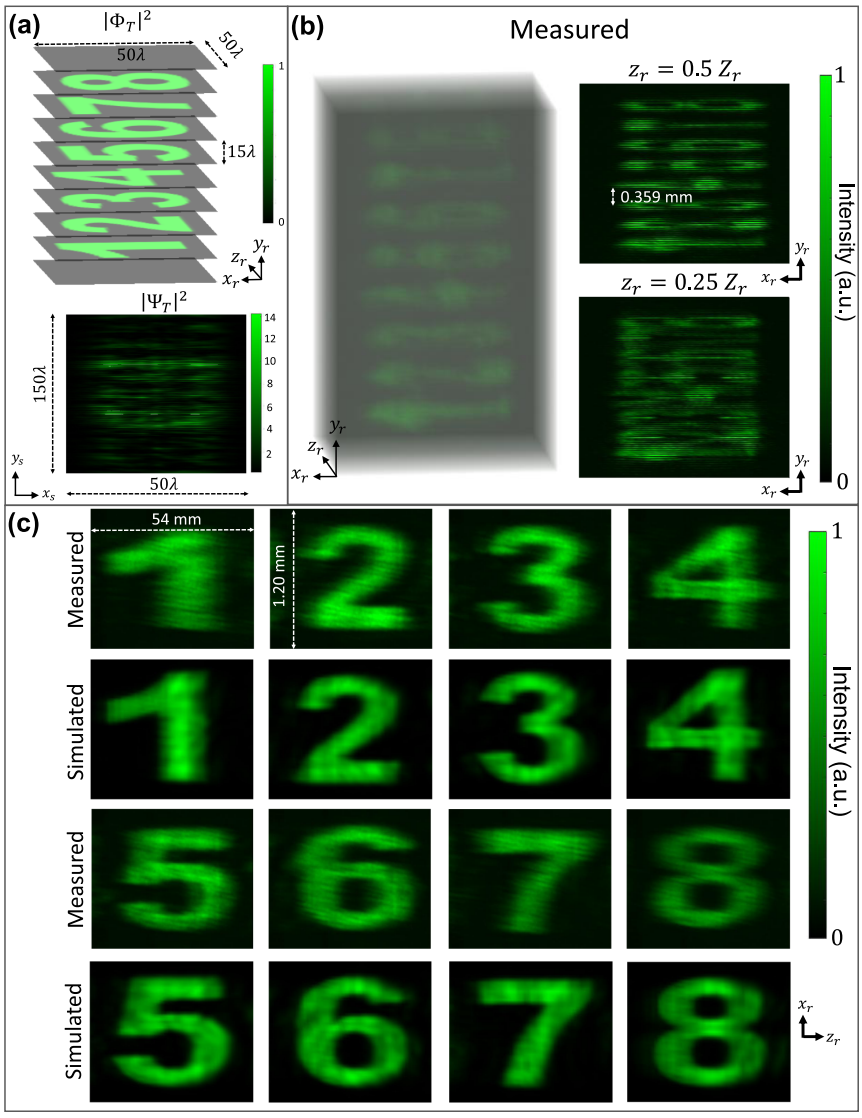

Fig. 5. Example of a 3D structured light wave projected in a set of uniformly spaced horizontal receiving planes. Projecting eight digits simultaneously at the eight inner horizontal receiving planes of the source-receiving space system of Fig. 1(c) with parameters listed in Table 1. (a) Target receiving profile $|\Phi_T|^2$ intensity and corresponding required source function $|\Psi_T|^2$ intensity computed using the first 3500 modes. (b) Optical reconstruction of the resulting wave using a phase-only SLM within a volume containing the horizontal receiving planes and at transverse planes located at the mid and quarter longitudinal distances, $z_r = Z_r/2$ and $z_r = Z_r/4$ (Z_r: longitudinal length of the planes). The wave solution is scaled up to match the utilized SLM display area and thus the 1:1 aspect ratio of the simulated wave is not preserved in the measured results. Measured spacing distance between the horizontal planes is $d_{y,r} = 0.359$ mm, while their dimensions are $Z_r \times X_r = 54$ mm $\times$ 1.20 mm. (c) Measured and simulated results of all eight reconstructed digits.

Our method reveals fundamental constraints in 3D field distributions that limit the reconstruction of a desired intensity profile, and, therefore, it can be used as a framework to tell us if a given 3D field distribution can be constructed or not. By projecting the target field onto the communication mode basis of the receiving volume, we assess whether it can be practically generated. Fields that require significant contributions from weakly coupled modes are infeasible, as they demand excessively large source amplitudes. This limitation stems from the rapid, quasi-exponential decay of coupling strengths—a fundamental property of wave physics associated with wave tunneling [64]—and is independent of source–receiver geometry. As a result, only well-coupled modes can be effectively used to generate fields within the volume. It is worth noting that once the communication modes are precomputed and stored, all subsequent calculations of the necessary source field and its resulting wave are done via linear matrix–vector multiplications and require no iterative refinement as we change the target profile. For the 3D light wave of Fig. 5, the time to compute its computer-generated hologram (CGH) is around 103 s, which can be further reduced using GPUs. By comparison, in the light-sheet method, the time to compute the CGH of the example shown in Supplementary Note 10 of Supplement 1 is around 8 min.

A limitation of our approach, on the other hand, is the high computation cost of initially calculating the communication modes for a given distribution. This may limit its applicability in scenarios where the receiving space itself is dynamic. The low diffraction efficiency, due to the use of a phase CGH encoding algorithm with low modulation depth, can also limit some applications. This can be mitigated by deploying another algorithm that balances diffraction efficiency and reconstruction

accuracy. We also note that our method relies on prior knowledge of Green's function between the source and receiving volume. In principle, for linear complex media, source and receiving modes differ from free-space modes by amplitude and phase shifts. These can, in theory, be determined via optimization techniques, such as power-maximizing orthogonal functions, as shown in planar systems in Ref. [72]. We reserve such analysis for another future work.

Creating time-reversed optical waves, with arbitrary amplitude, phase, and polarization at every point in space and time, can be used to control both linear and nonlinear optical phenomena [73]. Our approach can be extended to create those types of waves by adopting full time-dependent dyadic vector potential Green's function for the coupling operator [63]. In this case, metasurfaces [74,75] are an ideal wavefront shaping platform, as they offer multi-wavelength control and polarization transformations at the nanoscale [75]. In addition, the sub-wavelength regime of the flat-optics platform is also beneficial in creating reconstructed 3D light waves with higher resolution than the SLM. This extension can potentially unlock new applications in digital holography and structured light, as well as light–matter interaction, classical and quantum communications, and beyond.

6. METHODS

A. Communication Modes

The optimum orthogonal communication channels (modes) between two spaces using singular value decomposition were introduced in the optics literature in 1998 [59] and have led to many studies on how to maximize information transfer in wireless communications, optical fibers, and optical systems [60,63,76]. Notably, SVD modal optics has recently enabled integrated photonic processors to determine the most efficient waves to send information through arbitrary and scattering optical media [72], as theoretically predicted in Ref. [77]. In diffractive optics, the concept of communication modes was employed to analyze the resolution of one-dimensional optical systems in the Fresnel regime [61] and was also applied to an axicon geometry to study axial resolution [62].

In SVD modal optics, the source and receiving spaces are mathematically viewed as Hilbert spaces (H_S and H_R) that host the possible source and receiving eigenfunctions, $|\Psi_S\rangle$ and $|\Phi_R\rangle$, as illustrated in Fig. 1(a). The connection between these spaces is established through a coupling operator G_{SR}, which for free-space scalar waves can be described by Green's function [59]:

$$G_{SR,\lambda}(\mathbf{r}_R, \mathbf{r}_S) = -\frac{1}{4\pi}\frac{\exp(ik|\mathbf{r}_R - \mathbf{r}_S|)}{|\mathbf{r}_R - \mathbf{r}_S|}, \tag{1}$$

which maps a position $\mathbf{r}_S$ at the source space to a position $\mathbf{r}_R$ at the receiving space for a given operating wavelength λ. Such a scalar Green's function is usually sufficient for describing an electromagnetic wave of a single polarization. For cases of tight focusing or near-field behavior, or to use this approach for full vector fields, a similar approach can be taken using full dyadic Green's function [63]. In Eq. (1), $k = 2\pi/\lambda$ is the wave number, and a time harmonic dependence $\exp(-i\omega_0 t)$ is assumed, with $\omega_0 = kc$ being the operating angular frequency and c the light speed in free space. Following Ref. [63], we presume that the source space consists of N_S source points located at positions $\mathbf{r}_{S,j}$ $(j = 1, \ldots, N_S)$ while the receiving space contains N_R receiving points at positions $\mathbf{r}_{R,i}$ $(i = 1, \ldots, N_R)$, allowing us to describe G_{SR} as a $N_R \times N_S$ matrix:

$$g_{ij} = -\frac{1}{4\pi}\frac{\exp(ik|\mathbf{r}_{R,i} - \mathbf{r}_{S,j}|)}{|\mathbf{r}_{R,i} - \mathbf{r}_{S,j}|}. \tag{2}$$

The eigenfunctions $|\Psi_S\rangle$ and $|\Phi_R\rangle$ are found by solving the SVD of the coupling operator matrix G_{SR} of Eq. (2), which is equivalent to solving two eigenproblems, one associated with the operator $G_{SR}^{\dagger}G_{SR}$ and another one associated with $G_{SR}G_{SR}^{\dagger}$, leading to a one-to-one (injective) relation between these eigenfunctions and allowing us to establish the concept of a communication mode: a pair of eigenfunctions, one in the source space $|\Psi_{S,j}\rangle$ that couples to another one in the receiving space $|\Phi_{R,j}\rangle$, with the coupling strength of this connection given by the squared absolute value of the singular values s_j of G_{SR}, i.e., $|s_j|^2$ (see Supplementary Note 1 of Supplement 1). Each of these eigenfunctions is mathematically a column vector whose elements are the amplitudes at each different point in the appropriate space. Notice that $G_{SR}^{\dagger}G_{SR}$, described by a $N_S \times N_S$ matrix, is an operator within the source space, mapping a vector in H_S back to another vector in H_S. Similarly, $G_{SR}G_{SR}^{\dagger}$ is an operator within the receiving space, mapping from H_R back into H_R, being described by a $N_R \times N_R$ matrix. Since each of these two operators is a positive Hermitian operator, its eigenfunctions (or eigenvectors) are orthogonal and form a complete set for its Hilbert space, while its eigenvalues, given by the coupling strengths $|s_j|^2$, are positive real numbers. Moreover, the sets $\{|\Psi_{S,j}\rangle\}$ and $\{|\Phi_{R,j}\rangle\}$ constitute the optimum possible orthogonal channels connecting the two spaces in terms of the magnitude of the inner product. In other words, each receiving eigenfunction $|\Phi_{R,j}\rangle$ corresponds to the largest possible magnitude of the wave function its associated source eigenfunction $|\Psi_{S,j}\rangle$ can create at the receiving space. For further details about this maximization property, see Supplementary Note 1 of Supplement 1. Additionally, if the points are sufficiently dense in both spaces, this approach correctly converges toward the corresponding continuous functions and spaces, with convergence guaranteed by the Hilbert–Schmidt nature of Green's function operators for waves [63].

B. Synthesis of Light Fields

Given a target profile $|\Phi_T\rangle$, i.e., a vector of amplitudes at the receiving points, the required source function $|\Psi_T\rangle$ (vector of amplitudes at the source points) is determined by [32,63]

$$|\Psi_T\rangle = \sum_j \frac{1}{s_j}\langle\Phi_{R,j}|\Phi_T\rangle|\Psi_{S,j}\rangle, \tag{3}$$

where $\langle\Phi_{R,j}|\Phi_T\rangle$ is the projection of the target profile onto the set of receiving eigenfunctions (see Supplementary Note 1 of Supplement 1). The resulting wave created by the source function $|\Psi_T\rangle$ at a position $\mathbf{r}$ away from the source space is given by the sum of all the spherical waves emitted by the N_S source points weighted by $|\Psi_T\rangle$ [63]:

$$\phi(\mathbf{r}) = -\frac{1}{4\pi}\sum_{q=1}^{N_S}\frac{\exp(ik|\mathbf{r} - \mathbf{r}_{S,q}|)}{|\mathbf{r} - \mathbf{r}_{S,q}|}h_q, \tag{4}$$

where h_q is the qth component of $|\Psi_T\rangle$, such that $|\Psi_T\rangle = [h_1 \quad h_2 \quad \ldots \quad h_{N_S}]^T$.

C. Details on the Experimental Setup

We employed a 532 nm laser source, the Novanta Photonics Ventus Solid State CW laser. The reflective SLM is a SANTEC 200, with 1920 × 1200 pixel resolution and 8 μm pixel pitch. Before the SLM, the laser passes through a linear polarizer, then is focused by a 40X objective lens, spatially filtered by a 50 μm pinhole, and finally expanded and collimated using a 750 mm lens, resulting in a beam width ($1/e^2$) diameter of approximately 11 mm. This beam expander system provides a near-flat beam profile impinging on the utilized SLM display area, as our CGHs are designed under the assumption of a uniform illumination. The employed CCD camera is a μEye UI224SE-M, with 1280 × 1024 pixel resolution and 4.65 μm pixel size, mounted on a Thorlabs LTS150 translational z stage. The transverse profiles were recorded at each z plane with increments of 0.25 mm along the propagation direction.

Funding. Coordenação de Aperfeiçoamento de Pessoal de Nível Superior (88887.833874/2023-00); Conselho Nacional de Desenvolvimento Científico e Tecnológico (140270/2022-1, 309201/2021-7); Fundação de Amparo à Pesquisa do Estado de São Paulo (2020/05280-5); Office of Naval Research (N00014-20-1-2450); Air Force Office of Scientific Research (FA9550-21-1-0312, FA9550-22-1-0243); Optica.

Acknowledgment. The authors acknowledge the insightful discussions with Prof. M. Brongersma from Stanford University. V.S.A acknowledges financial support from the Coordination of Superior Level Staff Improvement (CAPES), grant no. 88887.833874/2023-00, and from the National Council for Scientific and Technological Development (CNPq), grant no. 140270/2022-1. A.H.D acknowledges the support of the Optica Foundation. L.A.A. acknowledges financial support from the National Council for Scientific and Technological Development (CNPq), grant no. 309201/2021-7, and from the São Paulo Research Foundation (FAPESP), grant no. 2020/05280-5. F.C. acknowledges financial support from the Office of Naval Research (ONR) under the MURI programme, grant no. N00014-20-1-2450, and from the Air Force Office of Scientific Research (AFOSR) under grant nos FA9550-21-1-0312 and FA9550-22-1-0243. D. M. also acknowledges support from AFOSR grant FA9550-21-1-0312.

Disclosures. The authors declare no competing interests.

Data availability. All key data supporting the findings of this study are included in the main article and its supplementary information. Additional data sets and raw measurements are available from the corresponding author upon reasonable request.

Supplemental document. See Supplement 1 for supporting content.

REFERENCES

1. J. Wang and Y. Liang, "Generation and detection of structured light: a review," Front. Phys. **9**, 263 (2021).
2. C. He, Y. Shen, and A. Forbes, "Towards higher-dimensional structured light," Light Sci. Appl. **11**, 205 (2022).
3. A. Laucht, F. Hohls, N. Ubbelohde, *et al.*, "Roadmap on quantum nanotechnologies," Nanotechnology **32**, 162003 (2021).
4. Z. Wan, H. Wang, Q. Liu, *et al.*, "Ultra-degree-of-freedom structured light for ultracapacity information carriers," ACS Photonics **10**, 2149–2164 (2023).
5. D. G. Grier, "A revolution in optical manipulation," Nature **424**, 810–816 (2003).
6. S. Kumar and R. Singh, "Recent optical sensing technologies for the detection of various biomolecules: review," Opt. Laser Technol. **134**, 106620 (2021).
7. M. Lee, H. Hugonnet, M. J. Lee, *et al.*, "Optical trapping with holographically structured light for single-cell studies," Biophys. Rev. **4**, 011302 (2023).
8. P. Genevet and F. Capasso, "Holographic optical metasurfaces: a review of current progress," Rep. Prog. Phys. **78**, 024401 (2015).
9. O. Quevedo-Teruel, H. Chen, A. Díaz-Rubio, *et al.*, "Roadmap on metasurfaces," J. Opt. **21**, 073002 (2019).
10. L. Huang, S. Zhang, and T. Zentgraf, "Metasurface holography: from fundamentals to applications," Nanophotonics **7**, 1169–1190 (2018).
11. Z. Wan, Z. Shi, Q. Liu, *et al.*, "Holographic tailoring of structured light field with digital device," Photonics **9**, 506 (2022).
12. H. B. Sedeh and N. M. Litchinitser, "Singular optics empowered by engineered optical materials," Nanophotonics **12**, 2687–2716 (2023).
13. A. I. Kuznetsov, M. L. Brongersma, J. Yao, *et al.*, "Roadmap for optical metasurfaces," ACS Photonics **11**, 816–865 (2024).
14. L. Allen, M. W. Beijersbergen, R. J. C. Spreeuw, *et al.*, "Orbital angular momentum of light and the transformation of Laguerre-Gaussian laser modes," Phys. Rev. A **45**, 8185–8189 (1992).
15. A. E. Siegman, "Hermite–Gaussian functions of complex argument as optical-beam eigenfunctions," J. Opt. Soc. Am. **63**, 1093–1094 (1973).
16. M. A. Bandres and J. C. Gutiérrez-Vega, "Ince–Gaussian beams," Opt. Lett. **29**, 144–146 (2004).
17. J. Pinnell, I. Nape, B. Sephton, *et al.*, "Modal analysis of structured light with spatial light modulators: a practical tutorial," J. Opt. Soc. Am. A **37**, C146–C160 (2020).
18. R. W. Gerchberg, "A practical algorithm for the determination of phase from image and diffraction plane pictures," Optik **35**, 237–246 (1972).
19. A. Forbes, M. de Oliveira, and M. R. Dennis, "Structured light," Nat. Photonics **15**, 253–262 (2021).
20. M. Piccardo, V. Ginis, A. Forbes, *et al.*, "Roadmap on multimode light shaping," J. Opt. **24**, 013001 (2021).
21. D. Leseberg, "Computer-generated three-dimensional image holograms," Appl. Opt. **31**, 223–229 (1992).
22. R. Piestun and J. Shamir, "Control of wave-front propagation with diffractive elements," Opt. Lett. **19**, 771–773 (1994).
23. J. Rosen and A. Yariv, "Snake beam: a paraxial arbitrary focal line," Opt. Lett. **20**, 2042–2044 (1995).
24. B. Salik, J. Rosen, and A. Yariv, "Nondiffracting images under coherent illumination," Opt. Lett. **20**, 1743–1745 (1995).
25. B. Salik, J. Rosen, and A. Yariv, "One-dimensional beam shaping," J. Opt. Soc. Am. A **12**, 1702–1706 (1995).
26. J. Rosen, B. Salik, and A. Yariv, "Pseudo-nondiffracting beams generated by radial harmonic functions," J. Opt. Soc. Am. A **12**, 2446–2457 (1995).
27. Y. Y. Schechner, R. Piestun, and J. Shamir, "Wave propagation with rotating intensity distributions," Phys. Rev. E **54**, R50–R53 (1996).
28. V. V. Kotlyar, V. A. Soifer, and S. N. Khonina, "An algorithm for the generation of laser beams with longitudinal periodicity: rotating images," J. Mod. Opt. **44**, 1409–1416 (1997).
29. U. Levy, D. Mendlovic, Z. Zalevsky, *et al.*, "Iterative algorithm for determining optimal beam profiles in a three-dimensional space," Appl. Opt. **38**, 6732–6736 (1999).
30. R. Piestun, B. Spektor, and J. Shamir, "Wave fields in three dimensions: analysis and synthesis," J. Opt. Soc. Am. A **13**, 1837–1848 (1996).
31. G. Shabtay, Z. Zalevsky, U. Levy, *et al.*, "Optimal synthesis of three-dimensional complex amplitude distributions," Opt. Lett. **25**, 363–365 (2000).
32. R. Piestun and J. Shamir, "Synthesis of three-dimensional light fields and applications," Proc. IEEE **90**, 222–244 (2002).
33. Y. Aborahama, A. H. Dorrah, and M. Mojahedi, "Designing the phase and amplitude of scalar optical fields in three dimensions," Opt. Express **28**, 24721–24730 (2020).
34. J.-H. Park, "Recent progress in computer-generated holography for three-dimensional scenes," J. Inf. Disp. **18**, 1–12 (2017).
35. D. Pi, J. Liu, and Y. Wang, "Review of computer-generated hologram algorithms for color dynamic holographic three-dimensional display," Light Sci. Appl. **11**, 231 (2022).
36. P. W. M. Tsang, T.-C. Poon, and Y. M. Wu, "Review of fast methods for point-based computer-generated holography [invited]," Photonics Res. **6**, 837–846 (2018).
37. Y. Zhang, H. Fan, F. Wang, *et al.*, "Polygon-based computer-generated holography: a review of fundamentals and recent progress [invited]," Appl. Opt. **61**, B363–B374 (2022).
38. M. Bayraktar and M. Özcan, "Method to calculate the far field of three-dimensional objects for computer-generated holography," Appl. Opt. **49**, 4647–4654 (2010).
39. N. Okada, T. Shimobaba, Y. Ichihashi, *et al.*, "Band-limited double-step Fresnel diffraction and its application to computer-generated holograms," Opt. Express **21**, 9192–9197 (2013).

40. Y. Zhao, L. Cao, H. Zhang, *et al.*, "Accurate calculation of computer-generated holograms using angular-spectrum layer-oriented method," Opt. Express **23**, 25440–25449 (2015).
41. J.-S. Chen and D. P. Chu, "Improved layer-based method for rapid hologram generation and real-time interactive holographic display applications," Opt. Express **23**, 18143–18155 (2015).
42. H. Zhang, L. Cao, and G. Jin, "Computer-generated hologram with occlusion effect using layer-based processing," Appl. Opt. **56**, F138–F143 (2017).
43. G. Makey, Ö. Yavuz, D. K. Kesim, *et al.*, "Breaking crosstalk limits to dynamic holography using orthogonality of high-dimensional random vectors," Nat. Photonics **13**, 251–256 (2019).
44. Y. Pang, A. Cao, J. Wang, *et al.*, "Simple encoding method of phase-only hologram for low crosstalk full-color multi-plane holographic projection," Opt. Lasers Eng. **147**, 106748 (2021).
45. A. Velez-Zea, J. F. Barrera-Ramírez, and R. Torroba, "Improved phase hologram generation of multiple 3d objects," Appl. Opt. **61**, 3230–3239 (2022).
46. Z. Wang, T. Chen, Q. Chen, *et al.*, "Reducing crosstalk of a multi-plane holographic display by the time-multiplexing stochastic gradient descent," Opt. Express **31**, 7413–7424 (2023).
47. J. Wang, J. Wang, J. Zhou, *et al.*, "Crosstalk-free for multi-plane holographic display using double-constraint stochastic gradient descent," Opt. Express **31**, 31142–31157 (2023).
48. M. Zamboni-Rached, "Stationary optical wave fields with arbitrary longitudinal shape by superposing equal frequency Bessel beams: frozen waves," Opt. Express **12**, 4001–4006 (2004).
49. T. A. Vieira, M. R. R. Gesualdi, and M. Zamboni-Rached, "Frozen waves: experimental generation," Opt. Lett. **37**, 2034–2036 (2012).
50. T. Čižmár and K. Dholakia, "Tunable Bessel light modes: engineering the axial propagation," Opt. Express **17**, 15558–15570 (2009).
51. A. H. Dorrah, M. Zamboni-Rached, and M. Mojahedi, "Controlling the topological charge of twisted light beams with propagation," Phys. Rev. A **93**, 063864 (2016).
52. A. H. Dorrah, N. A. Rubin, M. Tamagnone, *et al.*, "Structuring total angular momentum of light along the propagation direction with polarization-controlled meta-optics," Nat. Commun. **12**, 6249 (2021).
53. A. H. Dorrah, A. Palmieri, L. Li, *et al.*, "Rotatum of light," Sci. Adv. **11**, eadr9092 (2025).
54. A. H. Dorrah, N. A. Rubin, A. Zaidi, *et al.*, "Metasurface optics for on-demand polarization transformations along the optical path," Nat. Photonics **15**, 287–296 (2021).
55. L. A. Ambrosio, "Millimeter-structured nondiffracting surface beams," J. Opt. Soc. Am. B **36**, 638–645 (2019).
56. J. O. de Sarro and L. A. Ambrosio, "Surface beams resistant to diffraction and attenuation and structured at the millimeter scale," J. Opt. Soc. Am. B **38**, 677–684 (2021).
57. A. H. Dorrah, P. Bordoloi, V. S. de Angelis, *et al.*, "Light sheets for continuous-depth holography and three-dimensional volumetric displays," Nat. Photonics **17**, 427–434 (2023).
58. N. Asoudegi, A. H. Dorrah, and M. Mojahedi, "Deep learning-assisted light sheet holography," Opt. Express **32**, 1161–1175 (2024).
59. D. A. B. Miller, "Spatial channels for communicating with waves between volumes," Opt. Lett. **23**, 1645–1647 (1998).
60. D. A. B. Miller, "Communicating with waves between volumes: evaluating orthogonal spatial channels and limits on coupling strengths," Appl. Opt. **39**, 1681–1699 (2000).
61. A. Thaning, P. Martinsson, M. Karelin, *et al.*, "Limits of diffractive optics by communication modes," J. Opt. A **5**, 153 (2003).
62. A. Burvall, P. Martinsson, and A. T. Friberg, "Communication modes applied to axicons," Opt. Express **12**, 377–383 (2004).
63. D. A. B. Miller, "Waves, modes, communications, and optics: a tutorial," Adv. Opt. Photonics **11**, 679–825 (2019).
64. D. A. B. Miller, Z. Kuang, and O. D. Miller, "Tunnelling escape of waves," Nat. Photonics **19**, 284–290 (2025).
65. G. Lerosey, F. Lemoult, and M. Fink, "Beating the diffraction limit with positive refraction: the resonant metalens approach," in *Plasmonics and Super-Resolution Imaging* (Jenny Stanford, 2017), pp. 33–90.
66. V. Arrizón, U. Ruiz, R. Carrada, *et al.*, "Pixelated phase computer holograms for the accurate encoding of scalar complex fields," J. Opt. Soc. Am. A **24**, 3500–3507 (2007).
67. M. I. Álvarez-Castaño, A. G. Madsen, J. Madrid-Wolff, *et al.*, "Holographic tomographic volumetric additive manufacturing," Nat. Commun. **16**, 1551 (2025).
68. V. V. Kotlyar, S. N. Khonina, and V. A. Soifer, "Iterative calculation of diffractive optical elements focusing into a three-dimensional domain and onto the surface of the body of rotation," J. Mod. Opt. **43**, 1509–1524 (1996).
69. P. N. Bernal, P. Delrot, D. Loterie, *et al.*, "Volumetric bioprinting of complex living-tissue constructs within seconds," Adv. Mater. **31**, 1904209 (2019).
70. J. W. Goodman, *Introduction to Fourier Optics* (Roberts and Company, 2005).
71. C. Cremer and B. R. Masters, "Resolution enhancement techniques in microscopy," Eur. Phys. J. H **38**, 281–344 (2013).
72. S. SeyedinNavadeh, M. Milanizadeh, F. Zanetto, *et al.*, "Determining the optimal communication channels of arbitrary optical systems using integrated photonic processors," Nat. Photonics **18**, 149–155 (2024).
73. M. Mounaix, N. K. Fontaine, D. T. Neilson, *et al.*, "Time reversed optical waves by arbitrary vector spatiotemporal field generation," Nat. Commun. **11**, 5813 (2020).
74. N. Yu and F. Capasso, "Flat optics with designer metasurfaces," Nat. Mater. **13**, 139–150 (2014).
75. A. H. Dorrah and F. Capasso, "Tunable structured light with flat optics," Science **376**, eabi6860 (2022).
76. R. Piestun and D. A. B. Miller, "Electromagnetic degrees of freedom of an optical system," J. Opt. Soc. Am. A **17**, 892–902 (2000).
77. D. A. B. Miller, "Establishing optimal wave communication channels automatically," J. Lightwave Technol. **31**, 3987–3994 (2013).

143.107.234.49 2026-01-08 15:15:52